CATALYSIS

Ambient-pressure synthesis of ethylene glycol catalyzed by C_{60}-buffered Cu/SiO_2

Jianwei Zheng[1]†, Lele Huang[1]†, Cun-Hao Cui[1], Zuo-Chang Chen[1], Xu-Feng Liu[1], Xinping Duan[1], Xin-Yi Cao[2], Tong-Zong Yang[3], Hongping Zhu[1], Kang Shi[1], Peng Du[1], Si-Wei Ying[1], Chang-Feng Zhu[3], Yuan-Gen Yao[2], Guo-Cong Guo[2], Youzhu Yuan[1]*, Su-Yuan Xie[1]*, Lan-Sun Zheng[1]

Bulk chemicals such as ethylene glycol (EG) can be industrially synthesized from either ethylene or syngas, but the latter undergoes a bottleneck reaction and requires high hydrogen pressures. We show that fullerene (exemplified by C_{60}) can act as an electron buffer for a copper-silica catalyst (Cu/SiO_2). Hydrogenation of dimethyl oxalate over a C_{60}-Cu/SiO_2 catalyst at ambient pressure and temperatures of 180° to 190°C had an EG yield of up to 98 ± 1%. In a kilogram-scale reaction, no deactivation of the catalyst was seen after 1000 hours. This mild route for the final step toward EG can be combined with the already-industrialized ambient reaction from syngas to the intermediate of dimethyl oxalate.

Ethylene glycol (EG) is commonly used as antifreeze and feedstock for polyethylene terephthalate used in bottles and packaging (*1*). In contrast to the production of petroleum-derived EG (*2*), EG can also be produced from syngas (CO and, more recently, CO_2 mixed with H_2) (*3*, *4*). Direct hydrogenation of syngas toward EG requires high pressure (>100 bar) at 230°C but has a low yield (theoretically 57% and experimentally <7%) resulting from thermodynamic limitation of Gibbs free energy and side reactions (*5*, *6*). Two-step strategies starting from syngas through intermediate species such as dimethyl oxalate (DMO) are suitable for EG production (Fig. 1A and fig. S1) (*7*–*10*). The coupling of CO with methanol to make DMO has been safely industrialized with a Pd catalyst approaching its thermodynamic yield limit at ambient pressure (*11*–*13*). However, conversion of DMO to EG still requires elevated hydrogen (H_2) pressure (typically 20 to 30 bar) and temperature (200°C). High-pressure reactions with H_2 compressors present environmental and safety risks that could be addressed with efficient catalysts running at near-ambient pressure conditions (*4*).

A copper-chromium catalyst was originally applied in the DMO-to-EG reaction but was detrimental to human health and the environment, primarily owing to the toxicity of chromium. In addition, high H_2 pressure (30 bar) was required (*14*). Alternatively, a copper-silica (Cu/SiO_2) catalyst that selectively hydrogenates the DMO-to-EG reaction may be used (*15*–*18*); however, Cu/SiO_2 suffers from insufficient activity at low pressure as well as poor stability (*7*, *9*, *14*, *17*). Efforts have been primarily directed toward promoting the Cu/SiO_2 catalyst by adding promoters such as B, Zn, and Au to tailor the electronic density of Cu species or enhance metal-support interactions (*16*, *19*–*22*). However, these element-modified catalysts readily deteriorated in structure and did not perform well at low H_2 pressure (*7*, *23*). These kinds of elemental promoters increase the density of electron-deficient copper by irreversibly accepting electrons from copper. In contrast to elemental promoters, molecular promoters such as C_{60} and C_{70}—in addition to accepting electrons from copper—can also give electron feedback to the electron-deficient copper to render useful redox properties during the catalytic process. Electronic modification by C_{60} is practical in photovoltaics, but the buffering effect of C_{60} is rarely reported in catalysis (*24*, *25*).

We used C_{60} as an electronic buffer to balance the electronic density of active Cu species and overcome the restrictions imposed on conventional Cu catalysts. As shown in Fig. 1, B and C, the conventional Cu/SiO_2 catalyst without C_{60} had a low EG yield of 9.6%, but DMO could be almost completely converted to EG with a yield of 98 ± 1% with the C_{60}-buffered Cu/SiO_2 catalyst (C_{60}-Cu/SiO_2) at ambient H_2 pressure. No substantial limitations in mass and heat transfer were observed in the reaction system at gauge pressure (the pressure above outside ambient) of 1 bar that merely supplies the necessary driving force for substrate diffusion. The catalytic parameters are listed in table S1, and the H_2 pressure for the reaction is equal to gauge pressure plus ambient pressure (the same expression is used throughout this article). An H_2/DMO ratio greater than a stoichiometry ratio is commonly used in industry for a number of purposes, such as removal of excess heat to facilitate the exothermal DMO hydrogenation (ΔG = −31.07 kJ mol^{-1}). After accelerating the reaction conditions by increasing the weight liquid hourly space velocity (WLHSV) from 0.6 $g_{(DMO)}$ $g_{(Catalyst)}^{-1}$ $hour^{-1}$ (simplified as h^{-1} in the following text) at 1 bar to 8.4 $hours^{-1}$ at 30 bar, C_{60}-Cu/SiO_2 maintained high DMO conversion and EG selectivity, whereas at the high WLHSV of 8.4 $hours^{-1}$, the activity of the pristine Cu/SiO_2 catalyst dropped to only a trace yield of EG, and the incomplete hydrogenation product methyl glycolate (MG) was observed (figs. S2 and S3 and table S2).

Lower hydrogenation pressure increased the EG selectivity over the C_{60}-Cu/SiO_2 catalyst, which was 96.2% at 30 bar but 98.0% at 1 bar, and although 20 by-products formed at 30 bar, only 2 by-products were observed at 1 bar (fig. S4). The EG yield at 1 bar is close to the equilibrium limit (98.7%, fig. S5). The apparent activation barrier E_a of C_{60}-Cu/SiO_2 is much lower than that of Cu-SiO_2 by ~54 kJ mol^{-1} (Fig. 1D). The introduction of C_{60} apparently allows the Cu catalyst to activate substrates more efficiently (table S3) (*14*–*19*), and by contrast to those working in high pressures (>20 bar) of H_2 previously reported for the DMO-to-EG process, even in homogeneous pathways (*26*–*28*).

A scale-up experiment (Fig. 1E and fig. S6) with 12.0 g of C_{60}-Cu/SiO_2 was conducted under typical reaction conditions with H_2/DMO = 100 (v/v) and WLHSV = 0.6 $hours^{-1}$. The external mass diffusion cannot be neglected under ambient pressure as the Mears' criterion is >0.15 (table S1). The H_2 pressure was thus set at 3 bar to ensure sufficient substrate diffusion, and as compensation to the pressure, the H_2/DMO ratio was reduced from 200 (v/v) in the initial microscale experiments to 100 (v/v) in the scale-up experiment. For the first 32 hours in the scale-up DMO-to-EG experiment, the temperature was set at 190°C according to the microscale test. However, overhydrogenated by-products (ethanol and butanediols) were produced. The following temperature was set at 182°C with a fluctuation of ±8°C to sustain a high EG yield of >98% up to 1000 hours (Fig. 1E). As extrapolated along the statistics lines of DMO conversion (up to 100%) and EG selectivity (>98%), no decreased yield was observed even after 1000 hours. The spent catalyst can be reused and shows almost no aggregation for the Cu nanoparticles (NPs) therein (fig. S7).

Transmission electron microscopy (TEM), scanning transmission electron microscopy-electron diffraction (STEM-EDX), and line-scan electron energy loss spectroscopy (EELS) were used to establish the morphologic structures of the as-prepared Cu/SiO_2 and C_{60}-Cu/SiO_2 catalysts, as well as identify distributions of Cu and C_{60} in the catalysts (Fig. 2 and figs. S6 and S8 to S10). The samples contained dispersed Cu NPs with sizes ranging from 2 to

[1]State Key Laboratory of Physical Chemistry of Solid Surfaces, National Engineering Laboratory for Green Chemical Production of Alcohols-Ethers-Esters, Collaborative Innovation Center of Chemistry for Energy Materials (iChEM), College of Chemistry and Chemical Engineering, Xiamen University, Xiamen, China. [2]State Key Laboratory of Structural Chemistry, Fujian Institute of Research on the Structure of Matter, Chinese Academy of Sciences, Fuzhou, China. [3]Xiamen Funano New Materials Technology Co., Ltd., Xiamen, China.
*Corresponding author. Email: yzyuan@xmu.edu.cn (Y.Z.Y.); syxie@xmu.edu.cn (S.Y.X.)
†These authors contributed equally to this work.

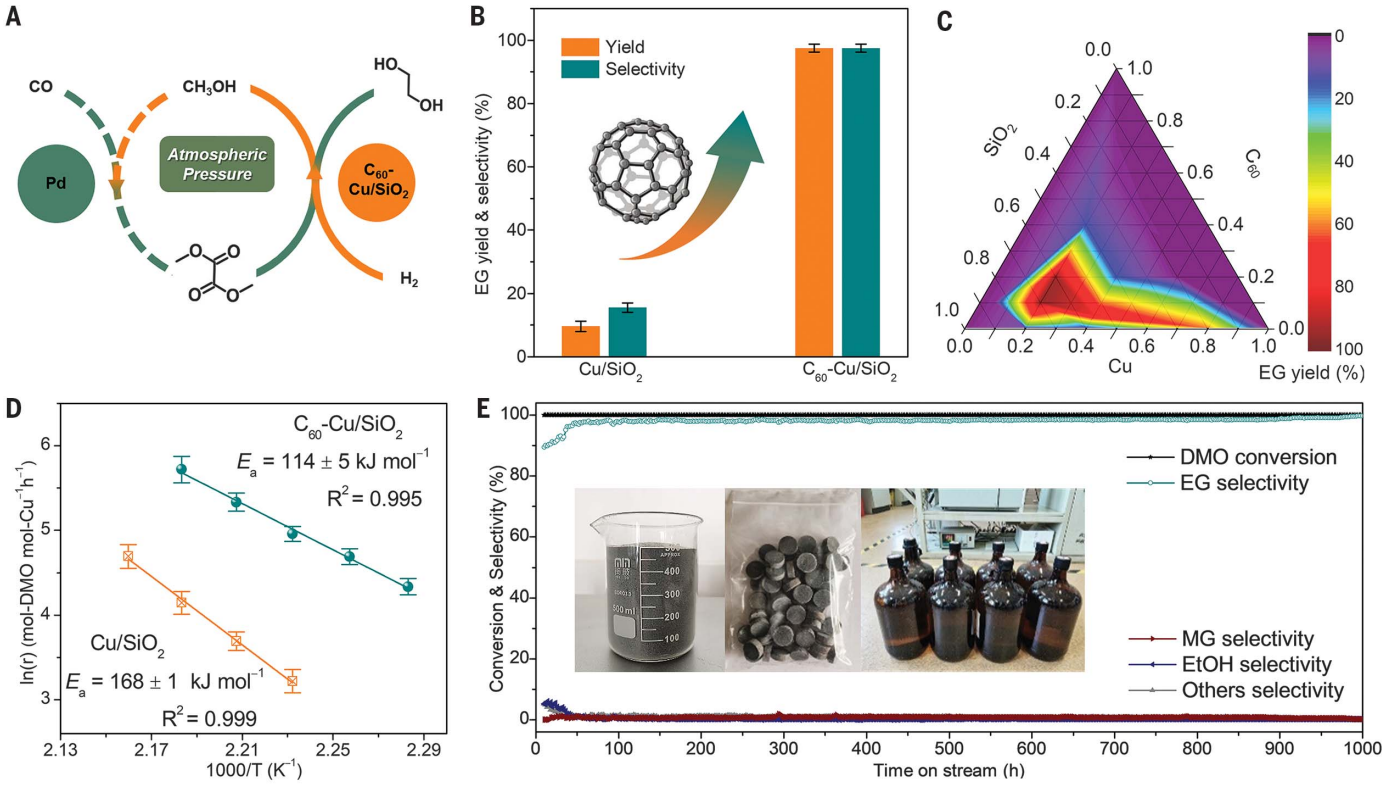

Fig. 1. Catalytical performance of Cu/SiO_2 and C_{60}-Cu/SiO_2 (C_{60}, 10 wt %; Cu, 20 wt %). (**A**) Scheme of the two-step approaches for the synthesis of EG from syngas through DMO hydrogenation. (**B**) Catalytic performance of Cu/SiO_2 improved by C_{60} at 1 bar, H_2/DMO = 200 (v/v, volume ratio), temperature 190°C, WLHSV 0.6 h^{-1}. (**C**) Two-dimensional contour snapshot of catalytic activity over xC_{60}-yCu-$zSiO_2$ ($x + y + z = 1$) with different formulations at 1 bar, H_2/DMO = 200 (v/v), temperature 190°C, WLHSV 0.6 h^{-1}. (**D**) Comparison of activation energy with Cu/SiO_2 and C_{60}-Cu/SiO_2 catalysts. (**E**) Stability tests in DMO hydrogenation with C_{60}-Cu/SiO_2 (scaled up to 12.0 g with the C_{60}-Cu/SiO_2 catalyst) at 3 bar, H_2/DMO = 100 (v/v), WLHSV 0.6 h^{-1}. Insets: catalyst powder (left), pellets (middle), and EG/methanol products (right).

Table 1. Catalytical performance of Cu/SiO_2 and C_{60}-Cu/SiO_2 for hydrogenation. C_{60} and Cu, 10 and 20 wt %, respectively. *P*, pressure; *T*, temperature; Δ*I*, performance improvement by C_{60} on the basis of the increment of yield.

Entry	Substrate	Product	*P*/bar	*T*/°C	WLHSV/h^{-1}	Catalyst	Yield/%	Selec./%	Δ*I*/%
1	Ethyl acetate	Ethanol	1	190	0.60	Cu/SiO_2	NIL	NIL	∞
						C_{60}-Cu/SiO_2	90.1	100.0	
2	Diethyl oxalate	Ethanol	1	240	0.60	Cu/SiO_2	47.7	47.7	80
						C_{60}-Cu/SiO_2	85.9	85.9	
3	Diethyl malonate	1,3-propanediol	30	190	0.60	Cu/SiO_2	8.8	21.4	620
						C_{60}-Cu/SiO_2	63.1	74.2	
4	Dimethyl succinate	butyrolactone	1	230	0.60	Cu/SiO_2	53.4	100.0	71
						C_{60}-Cu/SiO_2	91.6	94.9	
5	Dimethyl maleate	butyrolactone	1	240	0.60	Cu/SiO_2	72.6	100.0	32
						C_{60}-Cu/SiO_2	95.8	95.8	
6	Methyl lactate	1,2-propanediol	1	180	0.18	Cu/SiO_2	39.0	39.0	113
						C_{60}-Cu/SiO_2	83.2	83.2	
7	Methyl pyruvate	Methyl lactate	1	150	0.18	Cu/SiO_2	35.3	67.5	171
						C_{60}-Cu/SiO_2	95.5	95.5	
8	Methyl pyruvate	1,2-propanediol	1	180	0.18	Cu/SiO_2	6.3	8.4	1060
						C_{60}-Cu/SiO_2	72.7	72.7	

5 (nm). N_2O chemisorption in connection with H_2 pulse reduction was adopted to measure the exposed Cu surface area and dispersion (table S2). The Cu surface areas of Cu/SiO_2 and C_{60}-Cu/SiO_2 obtained are similar to each other (31 versus 34 m^2/g), consistent with observations of similar particle sizes (2.9 versus 3 nm) with TEM.

Thermogravimetric analysis in figs. S11 and S12 indicated that 90% of the C_{60} was successfully introduced for a loading of 10 wt % for C_{60}-Cu/SiO_2. Enlarged images of the NPs show C_{60} molecules anchoring on the surface of Cu NPs (Fig. 2, B and D, and fig. S9B). To estimate the distribution of C_{60} across the catalyst, the derivative of the thermogravimetric curve (fig. S12) was analyzed and the peak was deconvoluted at 380° to 540°C, attributed to C_{60} on the Cu surface. The data indicate that most of the C_{60} is loaded on the Cu surface (66% for C_{60}-Cu/SiO_2 with 10 wt % C_{60}) rather than on SiO_2.

X-ray diffraction patterns (XRD) of C_{60}-Cu/SiO_2 show diffraction peaks that can be assigned to C_{60} at 2θ = 10.8°, 17.7°, and 20.8°, corresponding to the (111), (220), and (311) planes, respectively. Additionally, the increasing intensities with progressive addition of C_{60} are shown in Fig. 2F and fig. S8 (*29*). Notably, the addition of C_{60} seems to preserve the Cu NPs surface structure because the physical parameters of metallic loading, NP size, pore structure, and specific surface area did not change

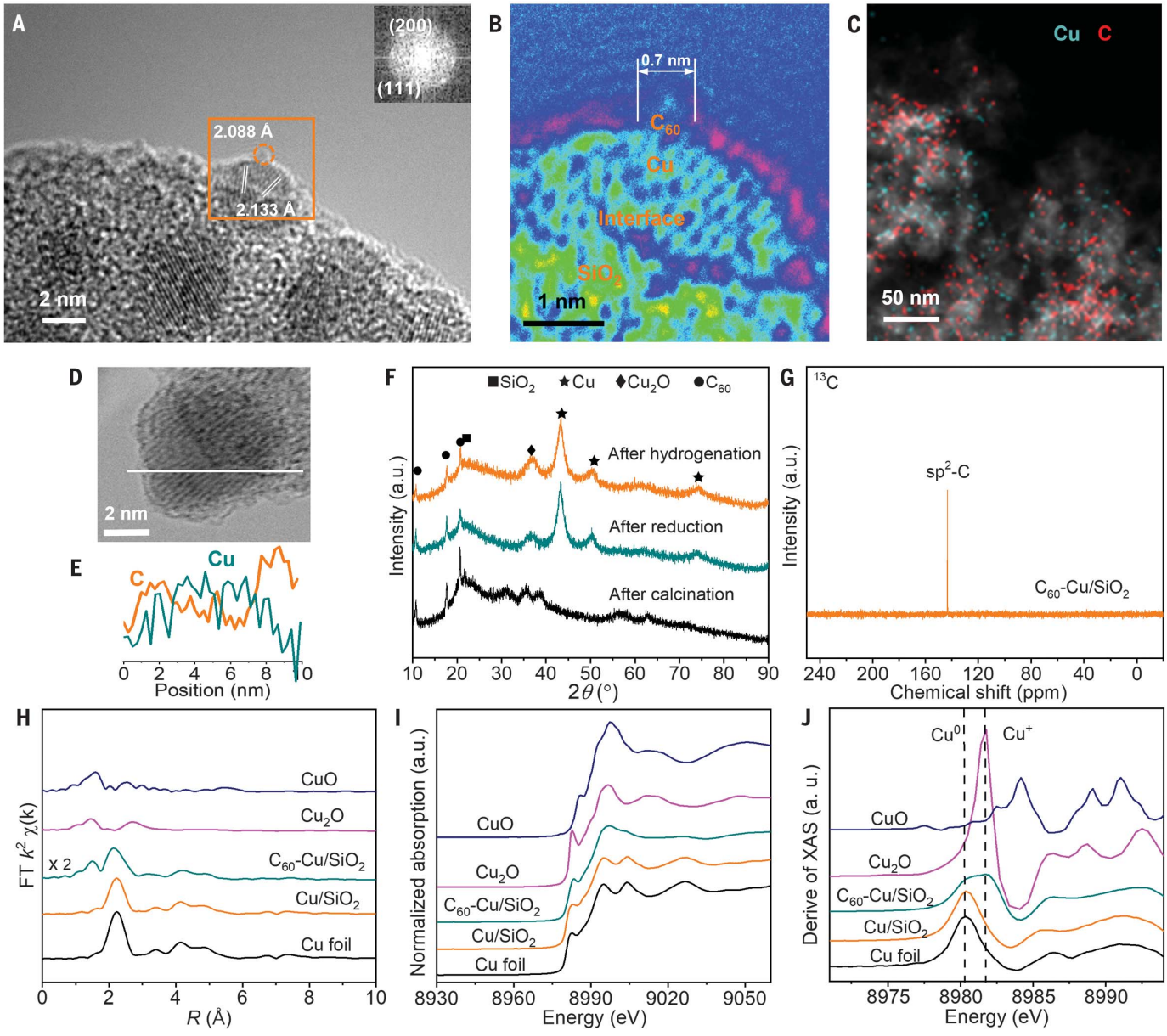

Fig. 2. Geometrical and electronic structural characterizations of C_{60}-Cu/SiO_2 (C_{60}, 10 wt %; Cu, 20 wt %). (**A**) Represented high-resolution TEM image of C_{60}-Cu/SiO_2. Inset: Fast Fourier Transform diffraction pattern of the square area. 2.133 and 2.088 Å are the lattice distances of Cu_2O and Cu species, respectively. (**B**) Color snapshot of the square in (A) showing a plausible C_{60} molecule sitting on a Cu NP. (**C**) Overlap of Cu and C elemental mapping on an SiO_2 matrix from EDX mapping; distribution of Cu is shown by cyan points and C species are shown by red points on the SiO_2 carrier (white frameworks). (**D**) Selected Cu nanoparticle. (**E**) Line EELS profiles in corresponding lines in (D). (**F**) XRD patterns of the C_{60}-Cu/SiO_2 catalyst after calcination, reduction, and hydrogenation reactions. (**G**) ssNMR of ^{13}C for C_{60}-Cu/SiO_2. (**H**) Fourier-transformed magnitudes of the experimental Cu *k*-edge EXAFS spectra. (**I**) Normalized Cu *k*-edge XANES spectra. (**J**) First derivative of Cu *k*-edge XANES spectra over Cu/SiO_2, C_{60}-Cu/SiO_2, CuO, Cu_2O, and Cu foil.

(table S2). Indeed, C_{60} is too big to intercalate into Cu lattice sites but appears to adsorb on the surface of Cu NPs through host-guest interactions. A line scan EELS profile through a Cu NP (Fig. 2, D and E) shows that the typical features of the surface species are carbonaceous and consistent with the spherical shape and subnanometer size of C_{60} adsorbed on Cu NPs. More microscopic images, as well as EELS profiles, are shown in the supplementary materials (figs. S9, B and C, and S10). H_2-temperature–programmed reduction (fig. S13) showed peaks shifting toward higher temperatures with the progressive addition of C_{60}, indicating that C_{60} can inhibit decorated Cu species from reduction.

To probe the chemical environment of the catalysts, solid-state NMR (ssNMR), x-ray absorption fine structure (XAFS), and x-ray absorption near-edge structure (XANES) characterizations were conducted for the catalysts as well as reference samples. As shown in Fig. 2G, only a sharp peak at 143.4 parts per million (ppm) attributed to sp^2-C of fullerene was observed in the ssNMR spectrum without sp^3-C signal (20 to 100 ppm) that would be associated with chemisorption of C_{60} on the Cu NPs. Fourier transform of extended XAFS spectra for C_{60}-Cu/SiO_2 (Fig. 2H and fig. S14) showed a peak at ~1.7 Å that we assigned to electron-deficient Cu species bonding with oxygen (*30*) or C_{60}, in addition to those corresponding to the Cu–Cu bond. Carbonaceous species were dispersed well with Cu in an interplay fashion by forming d–π interactions (fig. S15). The appearance of Cu–C scattering in C_{60}-Cu/SiO_2 implies possible interaction between C_{60} and Cu (table S4). Wavelet transform of XAFS spectra was indicated in fig. S15. Additionally, C_{60}-Cu/SiO_2 has two more lobes at (k, R) = (1.4, 2.2) and (4.0, 1.5), which could be attributed to the scatterings of Cu–C and Cu–O interaction, respectively. The former can be derived from d–π interactions between Cu and C_{60}, in accordance with the NMR without covalent bonding between the Cu and C. The possibility of observed coordinated d–π interactions between a Cu cluster and C_{60} has literature support from a previous crystallographic study (*31*).

XANES spectra in Fig. 2I show that the edge of C_{60}-Cu/SiO_2 falls between those of Cu foil and Cu_2O, demonstrating that Cu is multivalent. Similarly, first-derivative XANES (Fig. 2J) spectra showed a signature of Cu^0 and Cu^+ species for C_{60}-Cu/SiO_2, which was consistent with the result of Fourier transforms of the Cu k-edge XAFS oscillation in Fig. 2H. Cu^0 is the dominant species for the as-reduced Cu/SiO_2, whereas Cu^+ increases in C_{60}-buffered Cu/SiO_2, as evidenced by Auger electron spectroscopy (fig. S16).

To understand the catalytic role of the three constituents (namely C_{60}, Cu, and SiO_2) on

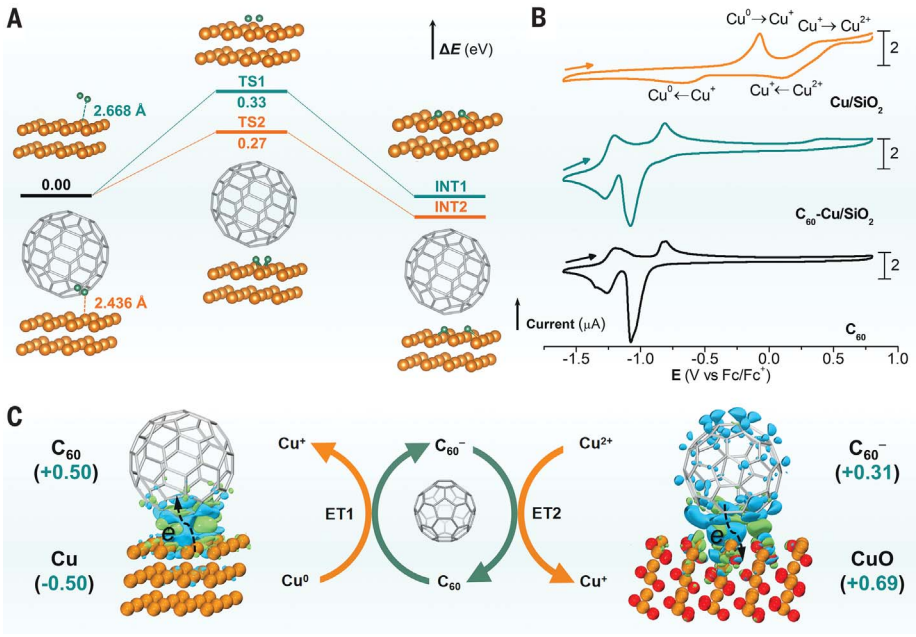

Fig. 3. Electron transfer in a Cu-based catalyst mediated by C_{60}. (**A**) Comparison of H_2 activation with C_{60}-Cu/SiO_2 and Cu/SiO_2 catalysts. TS and INT represent transition state and intermediate, respectively. The green and orange balls represent H and Cu, respectively. The distance between the Cu surface and H_2 is shortened from 2.668 to 2.436 Å when C_{60} is accommodated. (**B**) Cyclic voltammogram of Cu/SiO_2 (upper); C_{60}-Cu/SiO_2 (middle); and C_{60} (bottom) at 0.05 V s^{-1} in propylene carbonate solution containing 0.1 M tetrabutylammonium hexafluorophosphate and 0.016% v/v acetonitrile (segment of four–fifths cycle). All potentials were reported versus the redox couple of the internal ferrocene/ferrocenium (Fc/Fc^+) standard. The potential sweep starts at open circuit potential toward a cathodic direction; C_{60}, 10 wt %; Cu, 20 wt %. (**C**) Calculation results of Bader charges for C_{60}-Cu and C_{60}^--CuO surface interaction systems. The red and orange balls represent O and Cu atoms, respectively. ET represents electron transfer. The plus and minus represent the degree of the Bader charge. The overall Bader charge is 0 and 1 for C_{60}-Cu and C_{60}^--CuO, respectively. The green and blue areas with isosurface contours denote electron accumulation and electron depletion, respectively.

hydrogenation reactions, 20 samples of the C_{60}-Cu/SiO_2 catalysts with variable contents of C_{60}, Cu, and SiO_2 were synthesized and evaluated for the DMO-to-EG process at 1 bar and 190°C with 200 H_2/DMO and 0.6 $hours^{-1}$ WLHSV. As shown in the contour map (Fig. 1C) with EG yield varying as a function of chemical formulation, the highest activity was obtained for fractions between 0.2 to 0.4 for Cu, 0.6 to 0.8 for SiO_2, and 0.05 to 0.25 for C_{60}. Corresponding DMO conversion and EG selectivity have similar high activity compositions (fig. S2, B and C). Discussion of the catalytic roles of C_{60}, Cu, and SiO_2 is detailed in fig. S2 and in the supplementary text. These results imply that Cu is the primary active species for the heterogeneous hydrogenation of DMO and that the catalytic reactivity is sensitive to the addition of C_{60}.

For hydrogenation reactions in Cu-based catalysts, the dissociation of H_2 typically occurs on Cu metallic sites (*20*, *23*). We simulated the activation of H_2 on a crystalline Cu(111) surface and its combination with C_{60} by density functional theory (DFT). As shown in fig. S17, the introduction of C_{60} leads to local electronic redistribution and enhances the local charge density as electrons transfer from Cu to H atom(s) and C_{60} molecules. Meanwhile, the energy barrier for H_2 activation is lower because H_2 obtains more free electrons when coupling with C_{60}–Cu versus Cu alone. Temperature program desorption of H_2 coupled with mass spectrometry (H_2-TPD-MS) has been conducted to investigate the H_2–sorption capacity of the catalysts. As shown in fig. S18, all of the samples show desorption peaks at two regions (60° to 160°C and 300° to 600°C), corresponding to physical and chemical adsorption of H_2, respectively. Clearly, the introduction of C_{60} substantially promotes the chemical adsorption of H_2 as a significantly larger peak at 300° to 600°C. In addition, the bond length of Cu–H is shortened from 2.668 Å to 2.436 Å (Fig. 3A) when C_{60} is accommodated onto the Cu surface, indicating the enhancement of H_2 adsorption. The activation of DMO begins with the nucleophilic attack of adsorbed H atoms to the electron-deficient carbon of the ester group; further, promotion of H_2 activation on the Cu surface by C_{60} can further facilitate the activation of DMO on the Cu surface (*15*).

The theoretical models for C_{60}-Cu and C_{60}^--CuO systems were built to analyze the electron

transfers between C_{60} and Cu^0, C_{60}^- and Cu^{2+}. As shown in Fig. 3C, in the C_{60}-Cu system the Bader charge of Cu (−0.50) is more negative than that of C_{60} (+0.50), implying electron transfer (ET1) from Cu to C_{60}. By contrast, the Bader charge of CuO (+0.69) is higher than that of C_{60}^- (+0.31) in the C_{60}^--CuO system, indicating electron transfer from C_{60}^- to CuO (ET2). Therefore, C_{60} species are beneficial for stabilizing Cu^+.

To mimic electron transfer in dynamic redox processes of DMO hydrogenation over Cu-based catalysts mediated by C_{60}, we used cyclic voltammetry (CV) to transfer electrons to and from the catalyst. Fig. 3B shows the typical CV process of the Cu-based catalysts with or without C_{60} at a scan rate of 0.05 V s^{-1} in an electrolyte containing tetrabutylammonium hexafluorophosphate and propylene carbonate. Two pronounced anodic peaks around −0.2 and +0.3 V were observed for Cu/SiO_2 in the positive scan corresponding to the single-electron oxidation of Cu^0-to-Cu^+ and Cu^+-to-Cu^{2+} respectively. Correspondingly, two peaks in the negative scan around +0.2 and −0.6 V can be assigned to the reversible single-electron reduction of Cu^{2+}-to-Cu^+ and Cu^+-to-Cu^0, as detailed in Fig. 3B and fig. S19, A and B. By contrast, pure C_{60} in the solid state undergoes four redox peaks between −0.5 and −1.6 V (fig. S19C), which are two-step, one-electron–transfer reaction processes as reported previously (*32*).

For C_{60}-Cu/SiO_2, the peaks associated with single-electron oxidation of Cu^0-to-Cu^+ and single-electron reduction of Cu^{2+}-to-Cu^+ were completely absent, which we attributed to modulation of electron transfer by C_{60}. As supported by theoretical calculations for electron transfer between C_{60} and Cu surfaces (ET1, Fig. 3C), the electron lost from Cu^0 does not transfer to the electrode surface but is instead captured by C_{60}, and the current change is undetected in the external circuit. Similarly, the electrons from C_{60}^- can transfer back to Cu^{2+} (ET2, Fig. 3C), which reduced Cu^{2+} to Cu^+ without drawing electrons from the external circuit. Thus, C_{60} species, C_{60} and C_{60}^-, can act as a single-electron acceptor from Cu^0 or donate a single electron to Cu^{2+}, stabilizing Cu^+ and preventing transformation toward Cu^0 or Cu^{2+}.

For C_{60}-Cu/SiO_2, there was one anodic peak around +0.4 V in the positive scan and one cathodic peak around −0.8 V in addition to the peaks of C_{60}. On the basis of a series of electrochemical studies (fig. S19, D and E), we concluded that these two peaks could be assigned to oxidation of Cu^+-to-Cu^{2+} and reduction of Cu^+-to-Cu^0. Both peaks had weaker intensities and emerged at the voltages with higher positive or negative shifts than those of the pristine Cu/SiO_2, implying that it is more difficult to oxidize or reduce Cu^+ species with adsorbed C_{60}. Such a conclusion, regarding C_{60} acting as an electron buffer and creating a more stable environment for electron-deficient Cu species, is further supported by CV tests and DFT calculations on a molecular model of $Cu_{24}O_{24}Si_8R_8$ [R = (2,6-(i-C_3H_7)$_2$$C_6H_3$)N($SiMe_3$)] with a basic unit of Cu^+–O–Si (fig. S20) (*33*).

The improvement of C_{60} as an electron buffer to Cu/SiO_2 catalyst was further investigated for other hydrogenation reactions. As shown in Table 1, Cu/SiO_2 catalysts always show inferior activity compared with C_{60}-Cu/SiO_2. For example, no activity was observed over the Cu/SiO_2 catalyst during hydrogenation of ethyl acetate to ethanol, but the C_{60}-Cu/SiO_2 catalyst exhibited an ethanol yield of 90.1%. For 1,2-propanediol synthesis from methyl pyruvate, the improvement was more than an order of magnitude (6.3% versus 72.7%).

We note that most of the substrates in Table 1 can be derived from biomass, and selective hydrogenation is one of the most viable ways to use biomass. With C_{60}-Cu/SiO_2, the performance can be substantially improved, even under ambient pressure. In addition, C_{60} was recovered quantitatively from the catalysts (table S5). The recovered C_{60} was further confirmed using mass spectrometry (fig S21), indicating C_{60} was stable throughout the thermal process from calcination, reduction, and hydrogenation reactions. We have further explored the C_{60}-Cu/SiO_2 catalyst for electrochemical reduction of CO_2. The introduction of C_{60} to Cu/SiO_2 enhanced the faradaic efficiency of CO, and stability as shown in fig. S22. The excellent electrocatalytic reduction from CO_2 to CO endows the present work meaningful more to extend the CO_2-to-EG process overall at atmospheric pressure. Thus, the ambient-pressure hydrogenation of DMO catalyzed by C_{60}-Cu/SiO_2 reported could be applied to other thermo- and electrocatalytic reactions.

REFERENCES AND NOTES

1. K. Ravindranath, R. A. Mashelkar, *Chem. Eng. Sci.* **41**, 2197–2214 (1986).
2. S. Rebsdat, D. Mayer, "Ethylene glycol" in *Ullmann's Encyclopedia of Industrial Chemistry* (Wiley-VCH, 2000), pp. 531–544.
3. H. Yue, Y. Zhao, X. Ma, J. Gong, *Chem. Soc. Rev.* **41**, 4218–4244 (2012).
4. R.-P. Ye *et al.*, *ACS Catal.* **10**, 4465–4490 (2020).
5. J. F. Knifton, *J. Am. Chem. Soc.* **103**, 3959–3961 (1981).
6. T. Masuda, K. Murata, A. Matsuda, *Bull. Chem. Soc. Jpn.* **59**, 1287–1289 (1986).
7. J. Zheng *et al.*, *J. Phys. Chem. C* **119**, 13758–13766 (2015).
8. H. Miyazaki *et al.*, Ube, Japanese patent 57-180432 (1982).
9. H. Yue, X. Ma, J. Gong, *Acc. Chem. Res.* **47**, 1483–1492 (2014).
10. K. Dong *et al.*, *Nat. Commun.* **7**, 12075 (2016).
11. Z.-N. Xu *et al.*, *ACS Catal.* **3**, 118–122 (2013).
12. S.-Y. Peng *et al.*, *ACS Catal.* **5**, 4410–4417 (2015).
13. C. Wang *et al.*, *J. Catal.* **337**, 145–156 (2016).
14. G. Cui *et al.*, *Appl. Catal. B* **248**, 394–404 (2019).
15. C. Xu *et al.*, *Nat. Commun.* **9**, 3367 (2018).
16. Z. He, H. Lin, P. He, Y. Yuan, *J. Catal.* **277**, 54–63 (2011).
17. Y. Zhao *et al.*, *Ind. Eng. Chem. Res.* **59**, 12381–12388 (2020).
18. L.-F. Chen *et al.*, *J. Catal.* **257**, 172–180 (2008).
19. Y.-N. Wang *et al.*, *Catal. Sci. Technol.* **2**, 1637–1639 (2012).
20. J. Gong *et al.*, *J. Am. Chem. Soc.* **134**, 13922–13925 (2012).
21. Y. Huang *et al.*, *J. Catal.* **307**, 74–83 (2013).
22. M. M.-J. Li *et al.*, *Sci. Rep.* **6**, 20527 (2016).
23. H. Yue *et al.*, *Nat. Commun.* **4**, 2339 (2013).
24. G. Yu, J. Gao, J. C. Hummelen, F. Wudl, A. J. Heeger, *Science* **270**, 1789–1791 (1995).
25. L.-L. Deng, S.-Y. Xie, F. Gao, *Adv. Electron. Mater.* **4**, 1700435 (2018).
26. U. Matteoli, G. Menchi, M. Bianchi, F. Piacenti, *J. Mol. Catal.* **64**, 257–267 (1991).
27. H. T. Teunissen, C. J. Elsevier, *Chem. Commun.* **7**, 667–668 (1997).
28. X. Fang, C. Zhang, J. Chen, H. Zhu, Y. Yuan, *RSC Advances* **6**, 45512–45518 (2016).
29. K. Vimalanathan *et al.*, *Angew. Chem. Int. Ed.* **56**, 8398–8401 (2017).
30. J. Y. Kim, J. A. Rodriguez, J. C. Hanson, A. I. Frenkel, P. L. Lee, *J. Am. Chem. Soc.* **125**, 10684–10692 (2003).
31. S.-Z. Zhan *et al.*, *J. Am. Chem. Soc.* **142**, 5943–5947 (2020).
32. C. Jehoulet, Y. S. Obeng, Y. T. Kim, F. Zhou, A. J. Bard, *J. Am. Chem. Soc.* **114**, 4237–4247 (1992).
33. G. Tan, Y. Yang, C. Chu, H. Zhu, H. W. Roesky, *J. Am. Chem. Soc.* **132**, 12231–12233 (2010).
34. G. Kresse, J. Furthmüller, *Comput. Mater. Sci.* **6**, 15–50 (1996).
35. J. P. Perdew, K. Burke, M. Ernzerhof, *Phys. Rev. Lett.* **77**, 3865–3868 (1996).
36. W. Tang, E. Sanville, G. Henkelman, *J. Phys. Condens. Matter* **21**, 084204 (2009).
37. M. J. Frisch *et al.*, Gaussian 09, Revision A.02, (Gaussian Inc., 2016); https://gaussian.com/g09citation/
38. P. B. Weisz, C. D. Prater, *Adv. Catal.* **6**, 143–196 (1954).
39. S. T. Oyama, X. Zhang, J. Lu, Y. Gu, T. Fujitani, *J. Catal.* **257**, 1–4 (2008).
40. Q. Xie, F. Arias, L. Echegoyen, *J. Am. Chem. Soc.* **115**, 9818–9819 (1993).
41. Y. Yang *et al.*, *J. Am. Chem. Soc.* **117**, 7801–7804 (1995).
42. N. Ji *et al.*, *Angew. Chem. Int. Ed.* **47**, 8510–8513 (2008).
43. J. Sun *et al.*, *Sci. Adv.* **4**, eaau3275 (2018).
44. L. R. Zehner, R. W. Lenton, Atlantic Richfield Co., U.S. Patent 4112245 (1978).
45. R.-P. Ye *et al.*, *ACS Catal.* **8**, 3382–3394 (2018).
46. R.-P. Ye *et al.*, *J. Catal.* **350**, 122–132 (2017).
47. A. Satapathy, S. T. Gadge, B. M. Bhanage, *ACS Omega* **3**, 11097–11103 (2018).
48. A. Satapathy, S. T. Gadge, B. M. Bhanage, *ChemSusChem* **10**, 1356–1359 (2017).

ACKNOWLEDGMENTS

Funding: The work was supported by the National Natural Science Foundation of China (21721001, 92061000, 92061204, 21972113, 22171235, 21827801, 21972120, and 21703100), the National Key Research and Development Program of China (2017YFA0206801, 2017YFA0206802, and 2017YFB0307301), and the Strategic Priority Research Program of the Chinese Academy of Sciences (XDA21020800). We also thank XAS station (BL14W1) of the Shanghai Synchrotron Radiation Facility. **Author contributions:** J.W.Z. prepared, characterized, and tested the catalysts, and also wrote the manuscript draft. L.L.H., T.Z.Y., and X.F.L. amplified the synthesis. L.L.H. also organized the catalytic tests. Z.C.C and S.W.Y. performed the DFT calculations. C.H.C and K.S. performed the electrochemical study. X.P.D. and X.Y.C. participated in the early experiments. Y.G.Y. designed the scale-up experiments. H.P.Z. synthesized $Cu_{24}O_{24}Si_8R_8$. P.D. conducted CO_2 electrochemical reduction. G.C.G. developed DMO synthesis with Pd catalyst at ambient pressure. C.F.Z. synthesized C_{60} by arc-discharge of graphite. L.S.Z., S.Y.X., and Y.Z.Y. conceived the overall project. All coauthors discussed the data. **Competing interests:** The authors declare no competing interests. A patent has been filed by Xiamen University and Xiamen Funano New Materials Technology Co., Ltd on the findings reported here. **Data and materials availability:** All data are available in the main text or the supplementary materials.

SUPPLEMENTARY MATERIALS

science.org/doi/10.1126/science.abm9257
Materials and Methods
Supplementary Text
Figs. S1 to S22
Tables S1 to S5
References (*34*–*48*)

21 October 2021; accepted 25 January 2022
10.1126/science.abm9257

Ambient-pressure synthesis of ethylene glycol catalyzed by C_{60}-buffered Cu/SiO_2

Jianwei Zheng, Lele Huang, Cun-Hao Cui, Zuo-Chang Chen, Xu-Feng Liu, Xinping Duan, Xin-Yi Cao, Tong-Zong Yang, Hongping Zhu, Kang Shi, Peng Du, Si-Wei Ying, Chang-Feng Zhu, Yuan-Gen Yao, Guo-Cong Guo, Youzhu Yuan, Su-Yuan Xie, and Lan-Sun Zheng

Science, **376** (6590), .
DOI: 10.1126/science.abm9257

Promoting copper catalysts with C60

Ethylene glycol, a commodity chemical used as a feedstock and antifreeze agent, is synthesized industrially from dimethyl oxalate (DMO) by hydrogenation over precious-metal palladium catalysts at high pressures (typically 20 bars). Copper-chromium catalysts supported on silica as an alternative have required even high pressures. Zheng *et al*. show the addition of fullerene (C60) onto copper-silica allows DMO hydrogenation to be performed at ambient pressures with high yield (98%) and without deactivation after 1000 hours (see the Perspective by Gravel and Doris). The use of C60 to stabilize electron-deficient copper species that enhance hydrogen adsorption could likely be applied to other hydrogenation reactions catalyzed by copper. —PDS